MODELING BACTERIAL TRAVELING WAVE PATTERNS WITH EXACT CROSS-DIFFUSION AND POPULATION GROWTH

YONG-JUNG KIM AND CHANGWOOK YOON

Dedicated to the memory of Masayasu Mimura

Abstract. Keller-Segel equations are widely employed to explain chemotaxis-induced bacterial traveling band phenomena. In this system, the dispersal of bacteria is modeled by independently given diffusion and advection terms, and the growth of cell population is neglected. In the paper, we develop a chemotaxis model which consists of cross-diffusion and population growth. In particular, we consider the case that the diffusion and advection terms form an exact cross-diffusion. The developed mathematical models are based on the conversion dynamics between active and inactive cells with different dispersal rates. The process consists of three steps and the performance of each step is complemented by comparing numerical simulations and experimental data.

Introduction

The purpose of the paper is to develop a chemotaxis model that explains bacterial traveling wave patterns. In particular, Saragosti *et al.* [25] observed asymmetry in the traveling wave of Escherichia coli (see Figures 1 and 2) and developed a chemotaxis model that shows the asymmetry (solid lines in Figure 2) under the assumption that population growth is negligible. However, we focus on the main structure of the traveling wave pattern observed in Figure 2 that consists of a sharp pulse followed by a gentle bump. To do that the neglected population growth term should be included since the total population has been almost tripled in the experimental data.

In the paper, we take the reaction-diffusion system introduced by Mayan Mimura [19, (P_ε^μ)] as the base system and then develop it to a model that shows the traveling wave pattern in Figure 2 by adding chemotactic diffusion and a secondary resource such as oxygen. The process consists of three steps. The analysis of the base system are given in [20], but not the others. We will observe the properties of obtained models by numerically computing their solutions and comparing them to experimental data. We start with a discussion for classical chemotaxis models that describe bacterial traveling wave patterns.

Keller-Segel Equations. In their seminal paper [16] for chemotactic cell aggregation phenomena, Keller and Segel introduced an equation for cell population,

$$\rho_t = \nabla \cdot (\mu(\rho, v)\nabla\rho + \chi(\rho, v)\nabla v), \tag{1}$$

where ρ is the cell density, ρ_t is its partial derivative with respect to the time variable $t > 0$, v is the signaling chemical density, $\nabla\rho$ and ∇v are their gradients in the space, and $\mu(\rho, v)$ and $\chi(\rho, v)$ are respectively coefficients for diffusion and advection. Their choice of the coefficients in their paper [16] are

$$\mu(\rho, v) = \mu_0, \quad \chi(\rho, v) = -\chi_0\frac{\rho}{v}, \tag{2}$$

Date: August 18, 2022.

where μ_0 and χ_0 are positive constants. This model is called the logarithmic Keller-Segel model. Keller and Segel [17] also derived their chemotaxis model from a random walk system, which gives, for a function $\gamma(v)$,

$$\mu(\rho, v) = \gamma(v), \quad \chi(\rho, v) = (1 - \alpha)\gamma'(v). \tag{3}$$

In this model, α is the ratio of effective body length (i.e., distance between receptors) to step size of cell movement and $\alpha = 0$ corresponds to the case that the organisms do not sense the gradient ∇v. Another frequently used choice is

$$\mu(\rho, v) = \mu_0, \quad \chi(\rho, v) = -\chi_0\rho, \tag{4}$$

which is called the minimal Keller-Segel model. In these models, it is assumed that each cell of microscopic scale size senses and responds to macroscopic scale chemical gradients ($\alpha \neq 0$). Ever since the pioneering work by Keller and Segel, the chemotaxis theory has been developed under the assumption of sensing the chemical gradient, and various ways to sense the gradient have been studied (see [4, 23, 26]).

The same equation (1) is used to explain two different biological systems. The first one is for the aggregation phenomenon of myxamebae (see Bonner [3]). In fact, in their first chemotaxis paper [16], Keller and Segel modeled the cell aggregation phenomenon and took the second equation for the chemical density v as

$$v_t = D_v\Delta v + f(v)\rho - k(v)v, \tag{5}$$

where the signaling chemical v is produced by cells with production rate $f(v)$, diffused with diffusivity $D_v > 0$, and degraded with rate $k(v)$. The second biological system is for the traveling wave phenomenon of Escherichia coli (see Adler [1]). In their third chemotaxis paper [18], Keller and Segel modeled the traveling wave phenomenon and took the second equation for the chemical density v as

$$v_t = D_v\Delta v - k(v)\rho, \tag{6}$$

where v is the resource (or glucose) density and $k(v)$ is the consumption rate. Our focus of the paper is on the traveling wave patterns and we will mostly work with (6).

J. Adler introduced traveling a wave band of bacteria in his seminal paper [1] which is followed by a second traveling wave band. He showed that the phenomenon is related to the consumption of two resources, oxygen and galactose. After the first wave, the left over is consumed by the bacteria in the second wave band. The actual type and speed of the wave band depend on various conditions such as the resource density and viscosity (see [24]).

Recently, a structure of bacterial traveling bands is given in detail in Saragosti *et al.* [25]. Figures 1 and 2 are taken from the paper. In the paper, our task is to construct a mathematical model that explains these traveling wave patterns with biologically correct assumptions. Figure 1 shows that the traveling wave band propagates with a constant speed without changing the shape of the pulse front. We can also vaguely observe in the figure that, after the wave band passed, bacteria remain in a non-monotone pattern. The pattern of density distribution is more clearly given in Figure 2, where the time interval between snapshots is 2000s. The bacteria distribution in Figure 2 shows the propagation of a traveling wave band of a conserved shape with a constant speed followed by a second wave which is smaller than the first one and becomes wider as it propagates. The population growth of bacteria after the first wave band is also recently reported by Cremer *et al.* (see [7, Fig 4]). The specific speed and the pattern shape depend on the environment conditions.

In the rest of the paper, we will develop chemotaxis models in three steps to explain the patterns in Figure 2. Note that the Dirichlet boundary condition is given in Figure 2 at

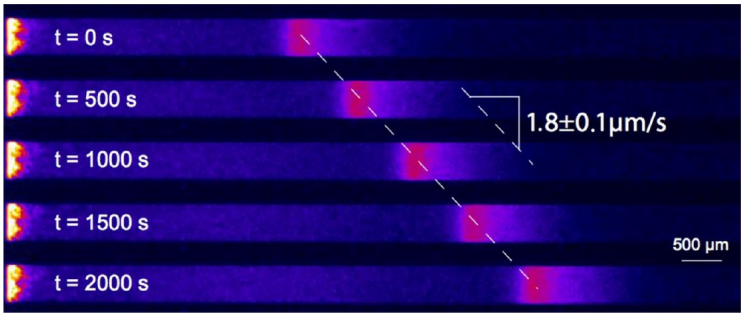

FIGURE 1. Experimental evidence for pulses fronts of Escherichia coli traveling across a channel with a constant speed.

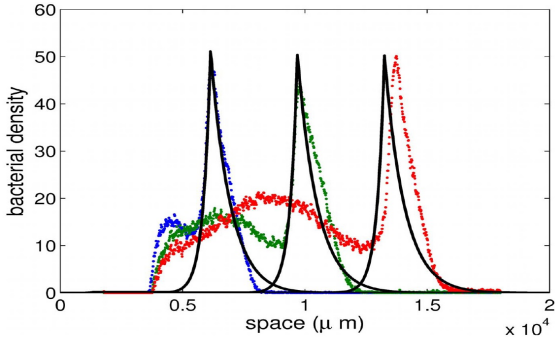

FIGURE 2. Experimental data (dots) and numerical results (solid lines) obtained by Saragosti *et al.* [25]. The time interval among the three snapshots is 2000s.(The two figures are from Saragosti *et al.* [25].)

approximately $x = 0.4$. However, to see the traveling wave phenomenon, we will consider the problem with the Neumann boundary condition. The doubling time of bacteria is usually between the 1200s (20 minutes) and 2400s (40 minutes). Since the time interval between the first and the third snapshots in Figure 2 is 4000s, a cell has enough time to be quadrupled. In Figure 2, the total mass of the bacteria is approximately tripled. Hence, the population dynamics is not negligible at all and plays a key role in the phenomenon. Including population dynamics is the first difference between our model and Keller and Segel's.

Chemotaxis models with exact cross-diffusion. The advection term $\chi(\rho, v)\nabla v$ in (1) is often called a *cross-diffusion* term since it gives dispersal effect against the gradient of the other component of the system. We will call it an *exact* cross-diffusion if

$$\partial_v \mu(\rho, v) = \partial_\rho \chi(\rho, v), \quad \rho, v \geq 0.$$

Then, there exists a potential function $F(\rho, v)$ such that the chemotaxis model (1) is written as

$$\rho_t = \Delta F(\rho, v). \tag{7}$$

If the ratio of effective body length is zero, i.e., $\alpha = 0$, Keller and Segel's model (1) with (3) is written as

$$\rho_t = \Delta(\gamma(v)\rho). \tag{8}$$

This is a case when the classical assumption that each individual bacterium detects a chemical gradient ∇v is dropped. Since the motility γ depends on v, this diffusion can be called a cross-diffusion. We may call it a cross-diffusion model in an exact form since there

is no extra advection term. Recently, chemotaxis models using a cross-diffusion term are actively studied. These models take (8) or its variation as the equation for the cell density and (5) or (6) as the equation for the resource or chemical density. Yoon and Kim [29] came up with the idea that the chemotactic traveling wave band can be explained without the gradient sensing assumption and then extended the idea to the aggregation model [30] (also see [2, 5, 9, 14, 28]). Jin, Kim, and Wang [15] extended the idea to the case with the logistic population dynamics (also see [12, 21, 22, 27]). One of the most critical steps in constructing such a diffusion model is how to choose the motility function which is often confusing. In this paper, we develop a method to construct the nonlinear motility function γ which gives the bacterial traveling band naturally.

Step 1. Singular limit for active and inactive cells

In the first step, we consider the singular limit of a reaction-diffusion system,

$$\begin{cases} a_t = d_a\Delta a + rna + \frac{1}{\varepsilon}(\beta(n)w - \alpha(n)a) & \text{in } Q_T, \\ w_t = \mu\Delta w + rnw + \frac{1}{\varepsilon}(\alpha(n)a - \beta(n)w) & \text{in } Q_T, \\ n_t = d_n\Delta n - n(a+w) & \text{in } Q_T, \\ \partial_\nu a = \partial_\nu w = \partial_\nu n = 0 & \text{on } \Gamma_T, \\ a(x,0) = a_0(x), \quad w(x,0) = w_0(x),\ n(x,t) = n_0(x) & \text{on } \Omega, \end{cases} \tag{9}$$

where $\Omega \subset \mathbb{R}^N$ with $N \geq 1$, $Q_T = \Omega \times (0,T)$, $\Gamma_T = \partial\Omega \times (0,T)$, and ν the outward unit normal vector on the boundary. The coefficients d_a, μ, and d_n are positive diffusivity constants. The coefficient $r > 0$ is the rate at which the consumed nutrient is converted into the bacteria population mass. The corresponding term models the population growth.

It is known well that bacteria become active when there are sufficient resources, and inactive otherwise (see [24, Figure 3] or [29, Figure 1]). In this model, we divide the cell population accordingly, where a and w are densities of active and inactive cells, respectively, and hence $\rho := a + w$ is the total cell density. The other component n is the density of a nutrient consumed by the bacteria. The coefficient $\alpha(n)$ is the rate that active cells convert to inactive ones. It is reasonable to assume this rate decreases if nutrient density n increases. The coefficient $\beta(n)$ is the rate that inactive cells convert to active ones which is assumed be an increasing function of the nutrient density. More specifically, the transition rates are assumed to satisfy

$$(H_{\alpha,\beta}) \qquad \begin{cases} \alpha, \beta \in C^1([0,\infty)) \cap L^\infty([0,\infty)), \\ \alpha(0) = \alpha_0, \quad \alpha'(n) \leq 0, \quad \text{and} \quad \alpha(n) > 0 \quad \text{for } n \geq 0, \\ \beta(0) = 0, \qquad \beta'(n) \geq 0, \quad \text{and} \quad \beta(n) > 0 \quad \text{for } n > 0. \end{cases}$$

The method of separating bacteria population into active and inactive cells has been successful in obtaining bacteria patterns (see [24]).

We may formally reduce the problem into a 2 equations reaction-diffusion system. First, after taking the limit as $\varepsilon \to 0$ with fixed $\mu > 0$, the limit of the solution should satisfy a relation

$$\beta(n)w = \alpha(n)a. \tag{10}$$

Adding the first two equations in (9) under the relation (10) gives

$$\begin{cases} \rho_t = \Delta(\gamma(n)\rho) + rn\rho & \text{in } Q_T, \\ n_t = d_n\Delta n - n\rho & \text{in } Q_T, \end{cases} \tag{11}$$

where $\rho = a + w$ is the total cell density and the motility $\gamma(n)$ is given by

$$\gamma = \frac{\mu\alpha(n) + d_a\beta(n)}{\alpha(n) + \beta(n)}\Big(= \gamma_1(n)\Big), \tag{12}$$

i.e., $\gamma(n)$ is an increasing function of the nutrient density n and is bounded below by $\mu > 0$ and above by d_a. Note that the diffusion of the total cell density is nonlinear and if $\mu < d_a$,

$$\gamma'(n) = \frac{(\mu - d_a)\beta\alpha' + (d_a - \mu)\alpha\beta'}{(\alpha + \beta)^2} > 0, \tag{13}$$

The system (11) with (12) is the 2 equations cross-diffusion model corresponding to the 3 equations linear system (9). The initial and boundary conditions are taken accordingly. The uniqueness of the weak solution of (11) and the convergence of the classical solution $(a_\varepsilon^\mu, w_\varepsilon^\mu, n_\varepsilon^\mu)$ of (9) to this unique solution as $\varepsilon \to 0$ are proved in [20]. Hence, the derivation from (9) to (11) is rigorous.

We will compare traveling wave solutions of the three equations system (9) and the two equations one (11) numerically. and will compare them with the experimentally obtained bacterial wave bands. Theoretical results exist only for the two equations system (11) in the one space dimension with $d_n = 0$. Then, (11) is written as

$$\begin{cases} \rho_t = (\gamma(n)\rho)_{xx} + rn\rho \\ n_t = -n\rho \end{cases} \qquad \text{for } x \in \mathbf{R},\ t > 0. \tag{14}$$

Note that the Keller-Segel model does not contain a growth term of the bacteria population and the traveling wave phenomenon is driven by the advection term only. However, (14) contains a population growth term and its traveling wave phenomenon is from the diffusion and the reaction together. We take a new space variable $\xi = x - ct$ for the moving frame with a constant wave speed $c > 0$. Then, the traveling wave solution, $(b(x,t), n(x,t)) = (b(x-ct), n(x-ct))$, satisfies

$$\begin{cases} c\rho' = -(\gamma(n)\rho)'' - rn\rho \\ cn' = n\rho \end{cases} \qquad \text{for } \xi \in \mathbf{R}, \tag{15}$$

where the notation $'$ denotes the differentiation with respect to ξ. We are looking for a traveling wave solution that satisfies boundary conditions,

$$\rho \to \rho_\pm \geq 0,\ n \to n_\pm \geq 0,\ \rho' \to 0,\ n' \to 0 \quad \text{as } \xi \to \pm\infty. \tag{16}$$

The existence, uniqueness, and the monotonicity of the traveling wave solution of (15) are given in [20]. The results are summarized as the following theorem.

Theorem ([20, Theorems 5.1 and 5.2]**)** Let $\rho_+ > 0$ and γ be given by (12) with $\mu \geq 0$ and $d_a > \mu$. (*i*) Suppose that there exists a smooth nontrivial traveling wave solution (ρ, n) of (15)–(16) with a wave speed $c > 0$. Then,

$$n_- = 0, \quad \rho_+ = 0, \quad \text{and} \quad \rho_- = rn_+ > 0, \tag{17}$$

and the nutrient density n is an increasing function.
(*ii*) If $\gamma''(n) \geq 0$, the total cell density ρ is a decreasing function.
(*iii*) Suppose that the boundary values satisfy (17). Then, there exists a nontrivial traveling wave solution (ρ, n) of (15)–(16) for all $c \geq c^*$, where the minimum wave speed is

$$c^* = 2\sqrt{r\gamma(n_+)n_+}. \tag{18}$$

The results in the theorem tell us the traveling waves obtained by the models (9) and (11) have the same properties that traveling wave solutions of Fisher-KPP type equations have. The equation for ρ in (11) is written as

$$\rho_t = \nabla \cdot (\gamma(n)\nabla\rho + \gamma'(n)\rho\nabla n),$$

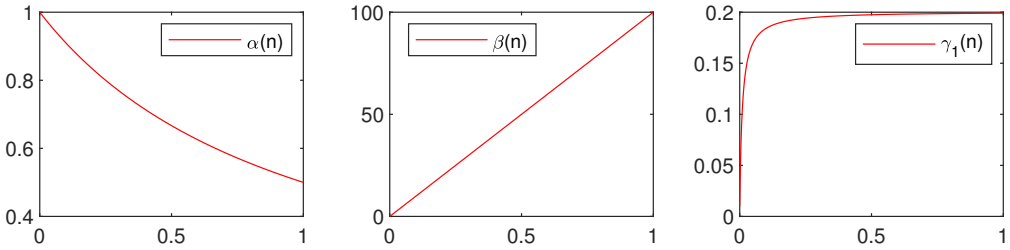

FIGURE 3. Graphs of transition rates and the motility γ_1 used in computations.

where $\gamma'(n) > 0$. Hence, the advection is against the nutrient and hence it does not give chemotactic movement toward resource.

Numerical simulations. Snapshots of a numerical solution of the 3 equations system (9) are given in Figure 4. For this computation, we took the transition rates as

$$\alpha(n) = \frac{1}{n+1}, \quad \beta(n) = \beta_0 n, \tag{19}$$

where the parameter β_0 is decided later (see Figure 3). We have chosen these transition rates simply because they are among the simplest ones that satisfy the hypotheses in $(H_{\alpha,\beta})$. However, the obtained motility functions γ in (21) or in (27) will give biologically meaningful results. In other words, the hypotheses in $(H_{\alpha,\beta})$ contain enough biological meaning for the bacterial traveling wave phenomena.

We take parameter values as

$$\varepsilon = 0.01, \quad d_a = 0.2, \quad \mu = 0.01, \quad d_n = 0.01, \quad r = 0.5, \quad \beta_0 = 100. \tag{20}$$

Then, the motility function γ in (12) is written as

$$\gamma(n) = \frac{\mu * \alpha(n) + d_a\beta(n)}{\alpha(n) + \beta(n)} = \frac{\mu + d_a\beta_0 n(n+1)}{1 + \beta_0 n(n+1)}. \tag{21}$$

The computation domain $\Omega = (L^-, L^+)$ is taken with $L^- = -5$ and $L^+ = 15$. The initial values are

$$a_0(x) = w_0(x) = 0, \quad n_0(x) = 1, \quad L^- < x < L^+. \tag{22}$$

The zero-flux Neumann boundary condition is taken

$$a_x(L^\pm, t) = n_x(L^\pm, t) = w_x(L^+, t) = 0, \quad t \geq 0, \tag{23}$$

where the subindexes such as a_x denotes partial derivative with respect to the space variable x. However, the boundary condition for w at L^- is the Dirichlet boundary condition,

$$w(L^-, t) = 0.5, \quad t \geq 0, \tag{24}$$

which is the steady state value when $a = 0$ and $n = 1$.

In the previous settings, the maximum nutrient density is $n_+ = 1$, and, if $n = n_+$, the ratio of the active cells over the inactive ones and the motility are

$$\frac{\beta(n_+)}{\alpha(n_+)} = \frac{\beta_0}{2} = 50, \quad \gamma(n_+) = \frac{\mu + 2d_a\beta_0}{1 + 2\beta_0} = 0.1991.$$

If the nutrient is consumed, i.e., if $n = n_- = 0$, we have

$$\frac{\beta(n_-)}{\alpha(n_-)} = 0, \quad \gamma(n_-) = \mu.$$

In Figure 3, the graph of the motility $\gamma(n)$ is given.

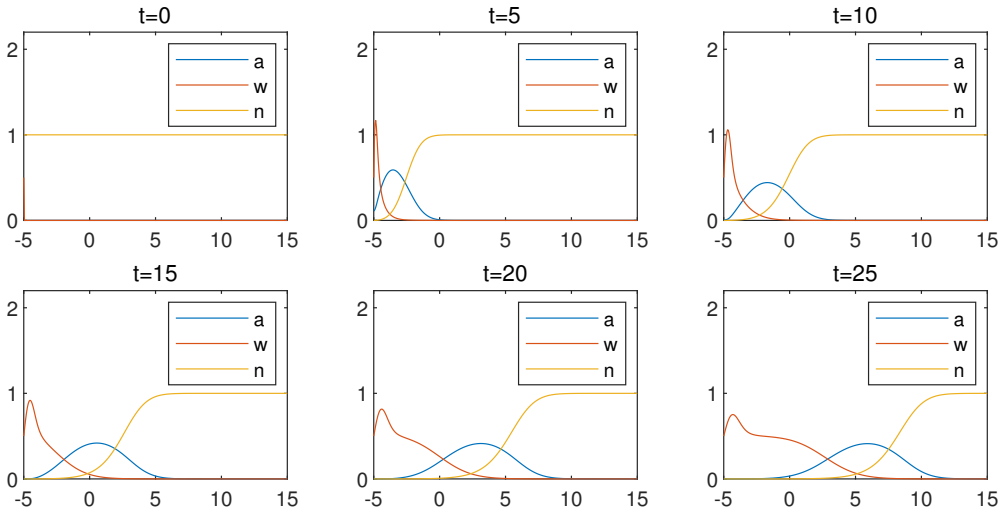

FIGURE 4. Snapshots of the solution of (9) with coefficients and boundary conditions in (20)–(24). Numerical wave speed is approximately $c = 0.561$.

The stability of the traveling wave solution of the problem is not proved. However, we may find from Figure 4 that the solution evolves to a traveling wave solution. The snapshot at time $t = 10$ shows that a band of active cells develops and then propagates with a constant speed. The profile for inactive cells is monotone decreasing except for the kink near the boundary at $x = L^-$. The kink is due to the initial condition and smears out slowly due to the small diffusivity $\mu > 0$ of inactive cells. The nutrient density n is monotone increasing. The wave speed obtained in Figure 4 is approximately $c = 0.561$. On the other hand, the minimum traveling wave speed of the problem (14) is

$$c^* = 2\sqrt{r\gamma(n_+)n_+} \cong 2\sqrt{0.5 \times 0.1991 \times 1} \cong 0.631,$$

which is greater than the wave speed observed in Figure 4. Note that this minimum wave speed is not for the three equations system (9), but for the simplified one (14), which corresponds to the case with $\varepsilon = d_n = 0$. Considering the difference between the two systems, the numerical wave speed is represented well by the minimum wave speed c^*.

The experimentally observed traveling wave patterns in Figure 2 are for the total population, and hence we need to see the traveling wave for the total cell population $a + w$. In Figure 5, snapshots of $a + w$ are displayed in the domain $x > 0$, not $x > -5$, to forget the initial effect of the kink. We can clearly see that the traveling wave is a front type, but not a pulse type. Finally, in Figure 6, snapshots of the solution of the 2 equations system (11) are displayed when the motility $\gamma(n)$ is given by (12) with parameters in (20) and (19). This is the singular limit of the system (9) as $\varepsilon \to 0$. For the comparison, the same initial value is taken as in Figure 4 with $\rho_0 = a_0 + w_0$. The boundary conditions for ρ are same as the ones for w. We can see that the snapshots of the two cases are indistinguishable. The numerical wave speed of the 2 equations system is approximately 0.571, which is slightly higher than the 3 equations system. Note that this limiting system corresponds to the case with $\varepsilon = 0$ and $d_n = 0.01 > 0$.

Pros and cons of the step 1 models. The 2 equations system (11)–(12) is a nonlinear model obtained as the singular limit of the 3 equations linear system (9) for active and inactive cells. Both active and inactive cells disperse with linear diffusion and the active cells have a larger dispersal rate than the one the inactive cells have, i.e., $d_a > \mu$. The comparison

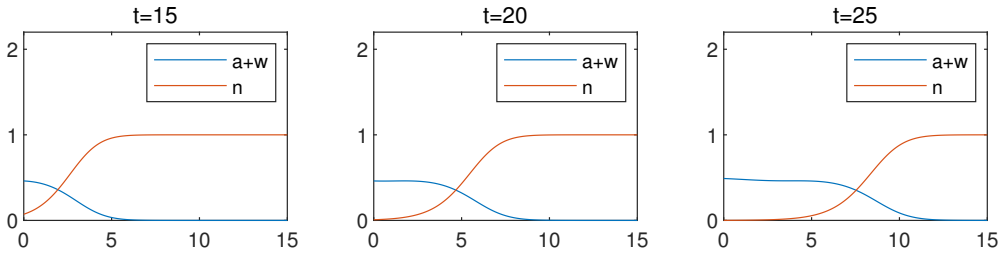

FIGURE 5. Snapshots of the total population $a + w$ for the step 1 model (9). Numerical wave speed is approximately $c = 0.561$.

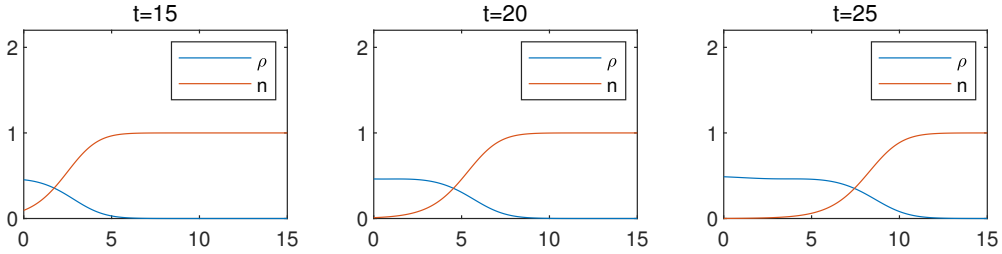

FIGURE 6. Snapshots of the step 1 cross-diffusion model (11). Numerical wave speed is approximately $c = 0.571$.

in Figures 5 and 6 shows that the reaction-diffusion system (11) with a nonlinear motility function in (12) shows the behavior of active and inactive cells correctly. The obtained cross-diffusion is a macroscopic view of a microscopic scale behavior of two phenotypes, where the method was introduced in [13] and then applied in other cases (see [8, 10, 11, 20]). The first contribution of step 1 is in obtaining the nonlinear motility given in (12) as an interaction between active and inactive cells.

The Keller-Segel equations explain chemotactic phenomena without population dynamics terms and show that the traveling wave phenomena of bacteria is due to chemotaxis mechanisms, but population one. However, if the goal is to explain the experiment patterns such as Figures 1 and 2, we need to properly include population dynamics terms. For example, the bacterial population is almost tripled in Figure 2. Recently, there are many research papers for the chemotaxis theory with logistic reaction terms (see [12, 15, 21, 22, 27]). The logistic reaction is proper to see long time phenomena in the ecology context. On the other hand, the reaction terms in (11) with conversion rate $r < 1$ is for short time phenomena. If the purpose of the model is to explain the pattern formation such as Figures 1 and 2, reaction terms in (11) is proper, not a logistic one. The second contribution of the step 1 is in introducing such a reaction term in a chemotaxis model.

The reaction-diffusion systems (9) and (11) show traveling wave phenomena clearly (see Figures 5 and 6). However, the obtained traveling wave is a front type, which is different from the pulse type traveling waves in Figures 1 and 2. Note that the traveling wave solution of the Fisher-KPP equation is also monotone which is similar to the ones in Figures 5 and 6. Therefore, we can only say that the traveling wave solutions of our first model (11) and the Fisher-KPP equation are not distinguishable. It is the fact that the traveling waves in Figures 1 and 2 are of pulse type that divides the chemotactic traveling waves from the Fisher-KPP ones. The first equation of the step 1 model (11) is written as

$$\rho_t = \nabla \cdot (\gamma(n)\nabla\rho + \gamma'(n)\rho\nabla n) + rn\rho,$$

where the advection term is against ∇n. This is the reason why the model (11) does not give a chemotactic traveling band. In the next step, we will see that if active cells take a chemotactic advection term, the pulse type traveling wave is obtained.

Step 2. Active cells with chemotactic behavior

Many biological organisms leave their habitat if starvation starts. Starvation-driven diffusion is a biological dispersal strategy that increases the dispersal rate when the resource becomes scarce (see [6]). We have seen that the solution of the step 1 model (9) does not give a pulse type traveling wave. In the Step 2 model, we will take a starvation-driven diffusion for active cells such as

$$a_t = \Delta(\phi(n)a),$$

where the motility $\phi(n)$ is a function of the nutrient n. The hypotheses on the motility function are

$$(H_\phi) \qquad 0 < \mu \le \phi(n), \quad \phi'(n) < 0.$$

In this case, the motility of active cells decreases if the amount of nutrient is abundant. This behavior gives chemotactic phenomena.

In the second step, we only replace the linear diffusion of active cells with the starvation-driven diffusion and consider

$$\begin{cases} a_t = \Delta(\phi(n)a) + rna + \frac{1}{\varepsilon}(\beta(n)w - \alpha(n)a) & \text{in } Q_T, \\ w_t = \mu\Delta w + rnw + \frac{1}{\varepsilon}(\alpha(n)a - \beta(n)w) & \text{in } Q_T, \\ n_t = d_n\Delta n - n(a+w) & \text{in } Q_T. \end{cases} \tag{25}$$

We do not change anything else and will see the effect of this chemotactic behavior of active cells. We can similarly derive a 2 equations system formally from (25). If we take the limit as $\varepsilon \to 0$ with a fixed $\mu > 0$, then the limit of the solution should satisfy a relation

$$\beta(n)w = \alpha(n)a.$$

If the first two equations in (25) are added, the sum $\rho = a + w$ satisfies

$$\begin{cases} \rho_t = \Delta(\gamma(n)\rho) + rn\rho & \text{in } Q_T, \\ n_t = d_n\Delta n - n\rho & \text{in } Q_T, \end{cases} \tag{26}$$

where

$$\gamma = \gamma_2(n) = \frac{\mu\alpha(n) + \phi(n)\beta(n)}{\alpha(n) + \beta(n)}. \tag{27}$$

The derivative of the motility γ consists of two parts,

$$\gamma'(n) = \frac{(\mu - \phi)\beta\alpha' + (\phi - \mu)\alpha\beta'}{(\alpha+\beta)^2} + \frac{\phi'\beta}{\alpha+\beta}. \tag{28}$$

The first part of the derivative is the one in (13) and is positive since $\phi(n) > \mu$. It is the second part which is newly added and is negative. If n is small, $\beta = \beta_0 n$ is small and hence the positive part dominates. If n is close to 1, β converges to β_0 and the positive part becomes small and $\gamma'(n)$ be comes negative (see Figure 7). If the resource becomes scarce, two scenarios are possible for active cells. An active cell may disperse more actively to find resource or become an inactive cell due to lack of resource. These two opposite behaviors are reflected in the graph of γ_2 which has the maximum at $n = 0.007$ approximately. On the other hand, we observe that $n \times \gamma_2$ is an increasing function.

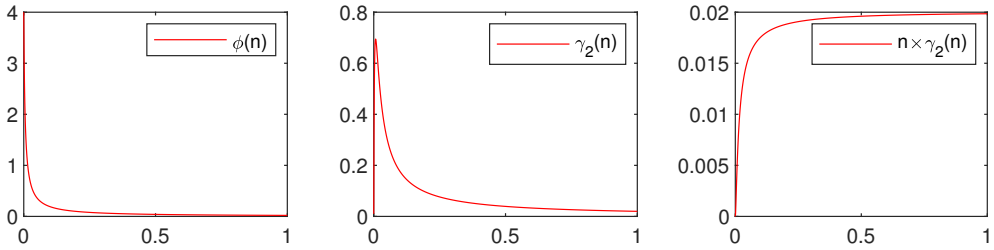

FIGURE 7. Graphs of $\phi(n)$ in (29), $\gamma_2(n)$ in (27), and $n \times \gamma_2(n)$.

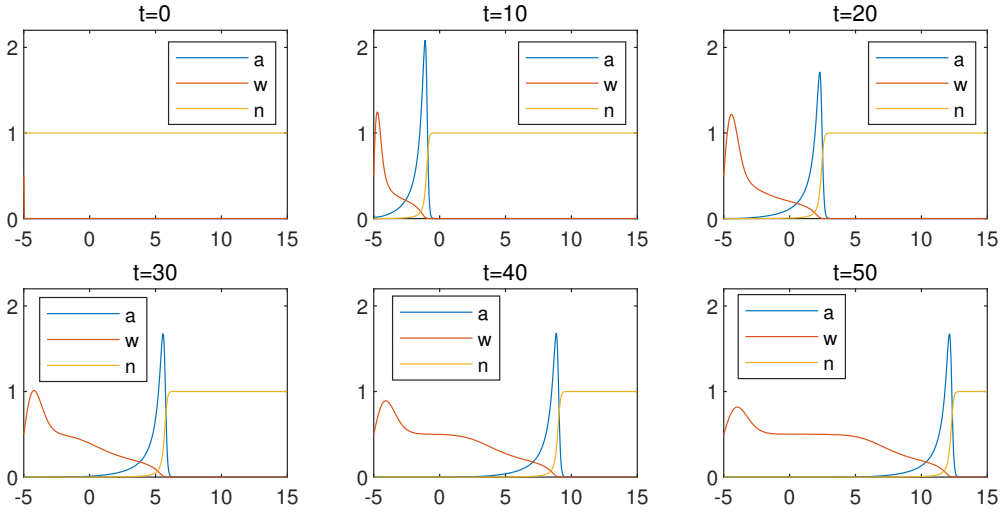

FIGURE 8. Snapshots of the solution of the step 2 model (25) with coefficients and boundary conditions in (20)–(24). Numerical wave speed is approximately $c = 0.328$.

The first equation of (26) is written as

$$\rho_t = \nabla \cdot \Big(\gamma(n)\nabla\rho + \frac{(\mu-\phi)\beta\alpha' + (\phi-\mu)\alpha\beta'}{(\alpha+\beta)^2}\rho\nabla n + \frac{\phi'\beta}{\alpha+\beta}\rho\nabla n \Big) + rn\rho.$$

The second advection term $\frac{\phi'\beta}{\alpha+\beta}\rho\nabla n$ is a new addition. Since $\phi'(n) < 0$, this second term gives a chemotactic behavior toward ∇n.

Numerical simulation. For the computation of (25) and (26), we took the same parameters in (20)–(19). The motility of active cells is taken as

$$\phi(n) = \frac{20}{1/d_a + 10n/\mu}, \tag{29}$$

where

$$\phi(0) = 20d_a \cong 4, \quad \phi(1) = \frac{20\mu d_a}{\mu + 10d_a} \cong 0.02, \quad \phi'(n) = \frac{-200/\mu}{(1/d_a + 10n/\mu)^2} < 0.$$

In the simulation, the nutrient density is bounded by $0 \le n \le n_+ = 1$. The wave speed is decided by the state $n = n_+$ as in (18) and $\phi(1)$ is one tenth of d_1. However, the chemotactic advection term increases the wave speed. The same initial and boundary conditions (22)–(24) are taken as the step 1 case.

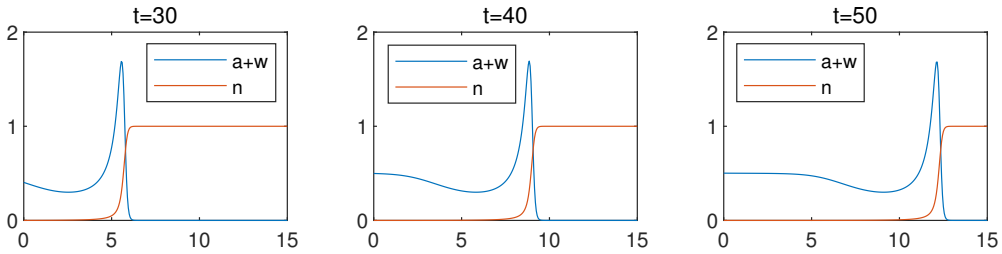

FIGURE 9. Snapshots of the total population $a + w$ for the step 2 model (25). Numerical wave speed is approximately $c = 0.328$.

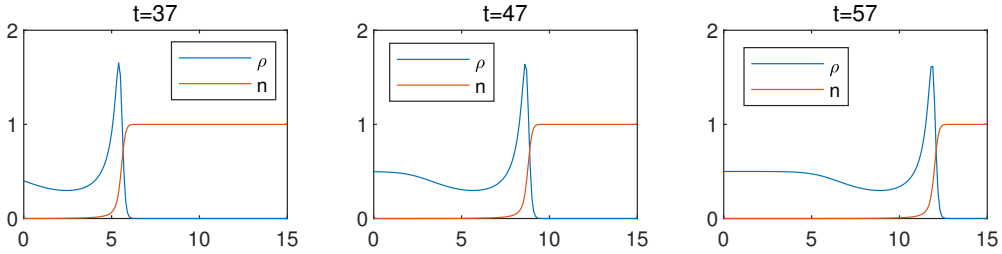

FIGURE 10. Snapshots of the step 2 singular limit model (26). Numerical wave speed is approximately $c = 0.322$.

Snapshots of the numerical solution of (25) are given in Figure 8. The wave pattern of inactive cells is still monotone decreasing except for the initial perturbation made at the domain boundary. The pattern for the nutrient density is still monotone increasing. However, the pulse-type wave pattern of active cells has changed drastically. It seems that the size of the active cell population is not changed much. However, the shape of the wave of the active cell density a is different from the one in step 1 case. It is asymmetric, taller, and narrower in comparison with the one in Figure 4. As a result of the change, the total population $a + w$ is not monotone anymore and the chemotactic diffusion of the active cells have broken the monotonicity of the wave pattern of the first step. The wave speed is approximately $c = 0.328$, which is a lot slower than the step 1 case. This speed reduction is due to the motility function of active cells given in (29).

The traveling wave pattern in Figure 2 corresponds to the total population. In Figure 9, snapshots for the total cell density $a + w$ are given in the domain $x > 0$. The pattern of the total cell population is a traveling pulse that takes two critical points. The maximum point is placed at the front of the propagation and a local minimum is placed after the peak is passed through. Finally, in Figure 10, snapshots of the solutions of the 2 equations system (26) are given when the motility $\gamma(n)$ is given by (27) and parameters by (20), (19), and (29). For the comparison, the same initial boundary conditions are taken as the ones for Figure 8 with $\rho_0 = a_0 + w_0$. We can see that the solutions are almost identical to the ones in (9). The shapes and the wave speeds of the two cases are almost identical to each other. There was a difference in the first stage of the solution where the trivial initial values are taken with non-trivial boundary conditions. This difference in the initial stage made a delay $\delta t = 7$ of appearance of the wave. However, except the initial stage, the two solutions evolve almost identically.

Pros and cons of the step 2 models. The success of the step 2 model is in obtaining a pulse-type traveling wave solution as was observed experimentally in Figures 1 and 2. Note that, in the step 2 model, the linear diffusion for active cells has been replaced with

a starvation-driven diffusion and other parts of the step 1 model are not changed at all. Hence, we may say that the pulse-type bacterial traveling wave phenomenon is induced by chemotaxis dynamics. The traveling wave solutions for Fisher-KPP type equations are monotone traveling waves. Hence, a traveling wave phenomenon itself is not an evidence for chemotactic dynamics, but it is the pulse-type traveling wave in Figure 9 that indicates the presence of chemotaxis. It is quite surprising that the 2×2 system (26) shows the same behavior of the 3 equations system (25) as in Figure 10. For the step 1 model case, the solutions are monotone and does not contain much information. However, we have pulse-type diffusion in the step 2 and the singular limit shows the exactly same traveling wave solution. This example shows the usefulness of the singular limit approach in obtaining the motility function γ.

Notice that fact that the motility function γ_1 in (12) is easily extended to the motility function γ_2 in (27). This is an advantage of using such chemotaxis model of Fokker-Planck type (8). Note that one may apply other chemotaxis dynamics such as Keller-Segel equations. Then, the first equation of (25) would be replaced by

$$a_t = \nabla \cdot (\phi(n)\nabla a - \chi(n)a\nabla n) + rna + \frac{1}{\varepsilon}(\beta(n)w - \alpha(n)a),$$

where the $\chi(n)$ and $\phi(n)$ are given independently. However, the resulting 2 equations singular limit system is not in such a simpler form and we did not pursue it.

Observe that the traveling wave pattern in Figure 2 shows an extra growth after the first pulse passed. Such an extra growth or the second traveling wave has been reported in many papers (see [1, 7]). It is known that the bacteria in the second wave consumes a secondary resource such as oxygen. The traveling wave in Figure 10 also shows such an extra growth. However, this is not due to the secondary resource, but due to the conversion from active cells to inactive cells. Hence, the secondary growth is smaller than the experimental data.

Step 3. Two types of resources

In the third step, we include a secondary resource for extra population growth and develop a 4×4 system. It is reported by Addler [1] that there are two wave bands of bacteria, where one mostly consumes oxygen and the other galactose. In the next model, we similarly assume that there exist two types of resources consumed by active and inactive cells. The model equations are

$$\begin{cases} a_t = \Delta(\phi(n)a) + rna + \frac{1}{\varepsilon}(\beta(n)w - \alpha(n)a) & \text{in } Q_T, \\ w_t = \mu\Delta w + rkmw + \frac{1}{\varepsilon}(\alpha(n)a - \beta(n)w) & \text{in } Q_T, \\ n_t = d_n\Delta n - na & \text{in } Q_T. \\ m_t = d_m\Delta m - kmw & \text{in } Q_T. \end{cases} \tag{30}$$

In this model, the resource n is consumed by active cells only with consumption rate 1. The density of the second resource is denoted by m and consumed by inactive cells with a consumption rate $k < 1$. The consumed resource turns into the bacteria mass and the conversion rate is $r < 1$. Except these two things, (30) is identical with (25).

We can similarly derive a 3 equations system formally from (30). If we take the limit as $\varepsilon \to 0$ with a fixed $\mu > 0$, then the limit of the solution should satisfy a relation

$$\beta(n)w = \alpha(n)a.$$

If the first two equations in (30) are added, the sum $\rho = a + w$ satisfies

$$\begin{cases} \rho_t = \Delta(\gamma(n)\rho) + \frac{rn\beta + rkm\alpha}{\alpha+\beta}\rho & \text{in } Q_T, \\ n_t = d_n\Delta n - \frac{n\beta}{\alpha+\beta}\rho & \text{in } Q_T, \\ m_t = d_m\Delta m - \frac{km\alpha}{\alpha+\beta}\rho & \text{in } Q_T, \end{cases} \tag{31}$$

where

$$\gamma = \gamma_2(n) = \frac{\mu\alpha(n) + \phi(n)\beta(n)}{\alpha(n) + \beta(n)}.$$

This is the final cross-diffusion chemotaxis model of the paper.

Numerical simulation. The step 3 model is the final one and we will see how close the bacterial traveling wave pattern obtained by the model is to the experimental data in Figure 2. For the computation of (30) and (31), we took the parameters as

$$\varepsilon = 0.01, \quad d_a = 0.2, \quad \mu = d_n = d_m = 0.01, \quad r = 0.5, \quad k = 0.2, \tag{32}$$

which are same as the ones in (20) except new parameters. The same transition rates in (19) and the same motility function in (29) are taken. However, we take initial values and boundary conditions differently to compare the computation patterns to Figure 2. First, the computation domain is $\Omega = (L^-, L^+)$ with $L^- = 0$ and $L^+ = 20$, which is slightly larger than the previous one. The initial values are given by

$$(a_0, w_0, n_0, m_0)(x) = \begin{cases} (\frac{1}{2}, 0, \frac{1}{2}, \frac{1}{2}), & 0 < x < 1, \\ (0, 0, 1, 1), & \text{otherwise.} \end{cases} \tag{33}$$

The zero-flux boundary condition is taken everywhere,

$$a_x(L^\pm, t) = n_x(L^\pm, t) = w_x(L^+, t) = m_x(L^\pm, t) = 0, \quad t \geq 0, \tag{34}$$

except the boundary condition for the inactive cells at L^-. We take the Dirichlet boundary condition for it, i.e.,

$$w(L^-, t) = 0.5, \quad t \geq 0. \tag{35}$$

Note that the boundary condition of the bacterial pattern in Figure 2 is the Dirichlet boundary condition at $x = 0.4$. Hence, we also took the Dirichlet boundary condition for w at $x = L^-$ for a comparison of the observed bacterial pattern and the simulated one.

Snapshots of the numerical solution of (30) are given in Figure 11. The active cell density a is a pulse type traveling wave. These pulses are similar to the ones of the step 2 model in Figure 8. In Figure 12, the snapshots for the total cell density $a + w$ are given. We can see that the front of the total cell density $a + w$ wave is in a pulse shape and the population slowly increases after the pulse passes by. This is the final bacterial traveling wave pattern of the paper which explains the pattern in Figure 2 nicely. Note that the parameter values of the numerical experiment are taken without experimental data. If the parameters are chosen with experimental measurement, it may give even a better match.

Discussions and Memories

The late Professor Mayan Mimura introduced the model system (9) to Y.-J. Kim and C. Yoon in 2016 as a mesoscopic-scale level bacterial behavior model that connects a microscopic-scale bacterial wave phenomenon to a macroscopic-scale cross-diffusion model. The original idea of the project was to show the singular limit of the solution of (9) as $\varepsilon \to 0$ with $\mu = 0$. In the accompanying modeling paper [20], we obtain the singular limits as $\varepsilon \to 0$ with $\mu > 0$ fixed and as $\mu \to 0$ as $\varepsilon > 0$ fixed. However, after the first round of discussions at Meiji University in 2017, the project was forgotten. One of the reasons

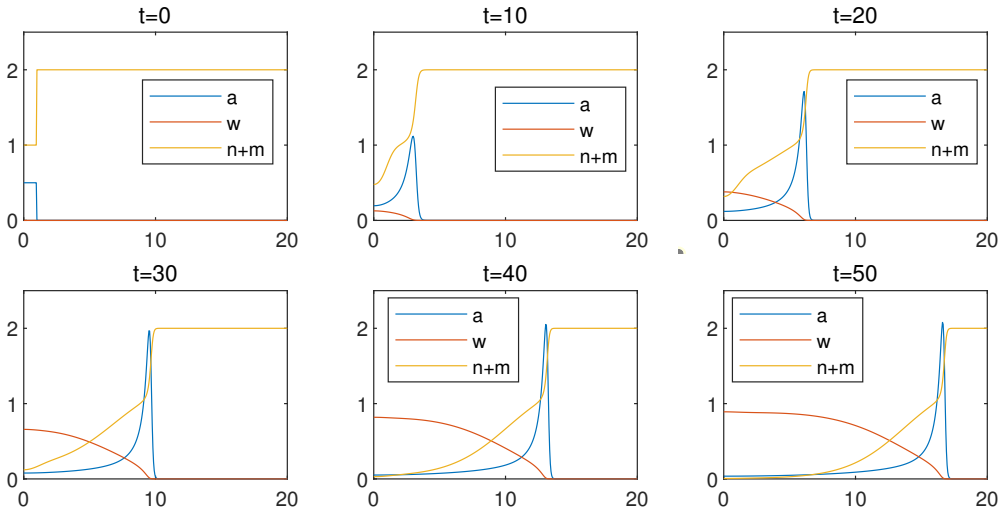

FIGURE 11. Snapshots of the solution of the step 3 model (30) with coefficients and boundary conditions in (32)–(35).

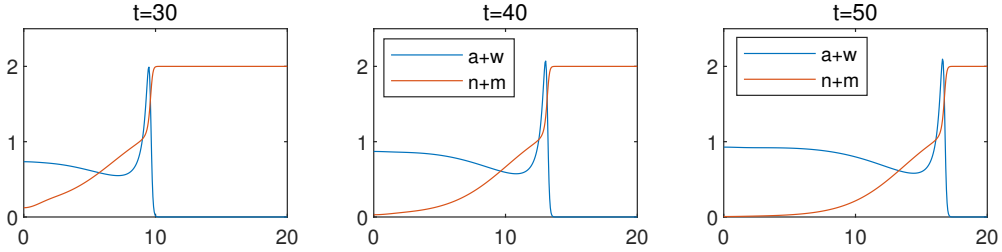

FIGURE 12. Snapshots of the total population $a + w$ for the step 3 model (30).

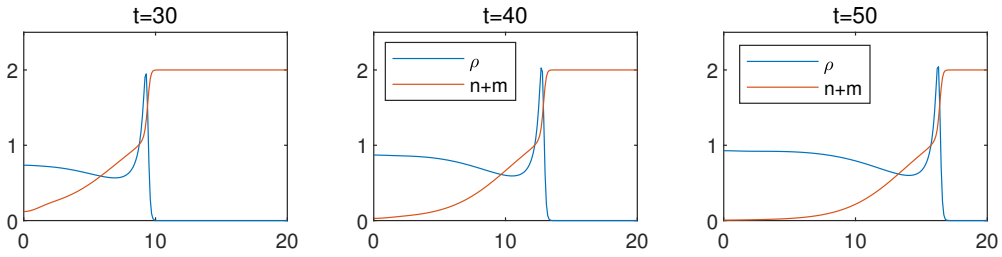

FIGURE 13. Snapshots of the total population $a + w$ for the step 3 model (31).

for forgetting the project was that the model provides monotone traveling waves, but not pulse-type traveling wave patterns. Recently, chemotaxis models with cross-diffusion in an exact form have been actively studied with or without population dynamics (see [5, 9, 12, 21, 22, 27, 28, 30]) and the authors realized that Mayan's idea may provide a theoretical background of such chemotaxis models. The project was brought back for this purpose and the authors realized that a simple addition of chemotactic diffusion to active cells completes the model and produces pulse-type bacterial patterns.

Let us return to the patterns in Figure 2. These experiment data take the zero-Dirichlet boundary condition. Hence, we also took the zero-Dirichlet boundary condition for the singular limit equation (31) of the step 3 model and displayed the distribution of the cell

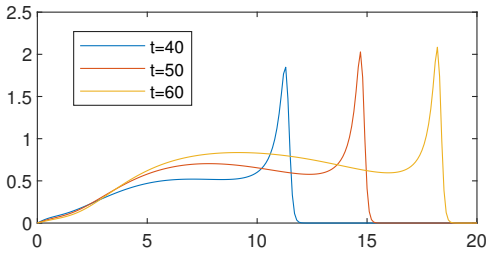

FIGURE 14. Bacteria pattern with Dirichlet boundary condition at $x = 0$

density ρ in Figure 14. This is the pattern that the final model (31) provides. Depending on the choice of parameters and the boundary condition one may have various patterns. Saragosti *et al.* [25] focused on the asymmetric pattern of the wavefront, where the pulse has a longer tail in the direction of propagation. However, the pattern in Figure 14 shows a shorter tail in the direction of propagation. One may apply a different motility function ϕ for the active cell. For example, the chemotaxis model developed in [25] can produce the asymmetric tail of the experimental data.

The two models (25) and (30) are designed with minimum changes of the base system (9) and we obtained desired final pattern from the modified model. It seems that the system (9) can be used as a base system to explain various phenomena. Mathematical analysis for the other two cases are not done yet. We need to see how far the analysis technique used in [20] can be extended to these modified systems.

ACKNOWLEDGEMENTS

Y.-J. Kim and C. Yoon were supported by National Research Foundation of Korea (NRF-2017R1A2B2010398 / NRF-2020R1I1A1A01074337).

REFERENCES

1. J. Adler. Chemotaxis in bacteria. *Science*, 153:708–716, 1966.
2. J. Ahn and C. Yoon. Global well-posedness and stability of constant equilibria in parabolic–elliptic chemotaxis systems without gradient sensing. *Nonlinearity*, 32(4):1327, 2019.
3. J.T. Bonner. *The Cellular Slime Molds*. Number 2nd Ed. Princeton University Press, 1967.
4. D.A. Brown and H.C. Berg. Temporal stimulation of chemotaxis in escherichia coli. *Proc. Natl. Acad. Sci.*, 71(4):1388–1392, 1974.
5. M. Burger, P. Laurençot, and A. Trescases. Delayed blow-up for chemotaxis models with local sensing. *arXiv:2005.02734 [math.AP]*, preprint, 2020.
6. E. Cho and Y.-J. Kim. Starvation driven diffusion as a survival strategy of biological organisms. *Bull. Math. Biol.*, 75:845–870, 2013.
7. J. Cremer, T. Honda, Y. Tang, J. Wong-Ng, M. Vergassola, and T. Hwa. Chemotaxis as a navigation strategy to boost range expansion. *Nature*, 575:658–663, 2019.
8. E. Crooks, E.N. Dancer, D. Hilhorst, M. Mimura, and H. Ninomiya. Spatial segregation limit of a competition-diffusion system with dirichlet boundary conditions. *Nonlinear Anal. Real World Appl.*, 5(4):645–665, 2004.
9. L. Desvillettes, Y.-J. Kim, A. Trescases, and C. Yoon. A logarithmic chemotaxis model featuring global existence and aggregation. *Nonlinear Anal. Real World Appl.*, 50:562–582, 2019.
10. Ján Eliaš, Danielle Hilhorst, Masayasu Mimura, and Yoshihisa Morita. Singular limit for a reaction-diffusion-ode system in a neolithic transition model. *J. Differential Equations*, 295:39–69, 2021.
11. Ján Eliaš, M Humayun Kabir, and Masayasu Mimura. On the well-posedness of a dispersal model for farmers and hunter–gatherers in the neolithic transition. *Math. Models Methods Appl. Sci.*, 28(02):195–222, 2018.
12. K. Fujie and J. Jiang. Global existence for a kinetic model of pattern formation with density-suppressed motilities. *J. Differential Equations*, 269(6):5338–5378, 2020.

13. T. Funaki, H. Izuhara, M. Mimura, and C. Urabe. A link between microscopic and macroscopic models of self-organized aggregation. *Netw. Heterog. Media*, 7:705–740, 2012.
14. J. Jiang and P. Laurençot. Global existence and uniform boundedness in a chemotaxis model with signal-dependent motility. *J. Differential Equations*, 299:513–541, 2021.
15. H.-Y. Jin, Y.-J. Kim, and . Wang. Boundedness, stabilization, and pattern formation driven by density-suppressed motility. *SIAM J. Appl. Math.*, 78:1632–1657, 2018.
16. E. Keller and L. Segel. Initiation of slime mold aggregation viewed as an instability. *J. Theor. Biol.*, 26:399–415, 1970.
17. E. Keller and L. Segel. Model for chemotaxis. *J. Theor. Biol.*, 30:225–234, 1971.
18. E. Keller and L. Segel. Traveling bands of chemotactic bacteria: A theoretical analysis. *J. Theor. Biol.*, 30:235–248, 1971.
19. Y.-J. Kim, Masayasu Mimura, and C. Yoon. Cross-diffusion modeling for bacterial traveling wave phenomenon. *Bull. Math. Biol.*, 2022.
20. Y.-J. Kim and C. Yoon. Nonlinear diffusion for bacterial traveling wave phenomenon. *Bull. Math. Biol.*, 2022.
21. W. Lv and Q. Wang. Global existence for a class of chemotaxis systems with signal-dependent motility, indirect signal production and generalized logistic source. *Z. Angew. Math. Phys.*, 71:53, 2020.
22. M. Ma, R. Peng, and Z. Wang. Stationary and non-stationary patterns of the density-suppressed motility model. *Physica D: Nonlinear Phenomena*, 402:132259, 2020.
23. R.M. Macnab and D.E. Koshland. The gradient-sensing mechanism in bacterial chemotaxis. *Proc. Natl. Acad. Sci.*, 69(9):2509–2512, 1972.
24. M. Matsushita, J. Wakita, H. Itoh, K. Watanabe, T. Arai, T. Matsuyama, H. Sakaguchi, and M. Mimura. Formation of colony patterns by a bacterial cell population. *PHYSICA A*, 274(1-2):190–199, 1999.
25. J. Saragosti, V. Calvez, N. Bournaveas, A. Buguin, P. Silberzan, and B. Perthame. Mathematical description of bacterial traveling pulses. *PLoS Comput. Biol.*, 6:1000890, 2011.
26. N. Vladimirov and V. Sourjik. Chemotaxis: how bacteria use memory. *Biological Chemistry*, 390(11):1097–1104, 2009.
27. J. Wang and M. Wang. Boundedness in the higher-dimensional keller-segel model with signal-dependent motility and logistic growth. *J. Math. Phys.*, 60:011507, 2019.
28. M. Winkler. Can simultaneous density-determined enhancement of diffusion and cross-diffusion foster boundedness in keller–segel type systems involving signal-dependent motilities? *Nonlinearity*, 33(12):6590–6623, 2020.
29. C. Yoon and Y.-J. Kim. Bacterial chemotaxis without gradient-sensing. *J. Math. Biol.*, 70(6):1359–1380, 2015.
30. C. Yoon and Y.-J. Kim. Global existence with pattern formation in cell aggregation model. *Acta. Appl. Math.*, 149:101–123, 2017.

(Yong-Jung Kim)
Department of Mathematical Sciences, KAIST, Daejeon 34141, Republic of Korea
Email address: yongkim@kaist.edu

(Changwook Yoon, Corresponding Author.)
Department of Mathematics Education, Chungnam National University, Daejeon 34134, Republic of Korea
Email address: chwyoon@cnu.ac.kr